Solar Physics
DOI: 10.1007/•••••-•••-•••-••••-•

High-Energy Emission from a Solar Flare in Hard X-rays and Microwaves

M.R. Kundu[1] · **E.J. Schmahl**[1,2] · **S.M. White**[1] · **V.V. Grechnev**[3] · **N.S. Meshalkina**[3] · **L.K. Kashapova**[3]

Abstract

We discuss one large flare using simultaneous observations obtained with two instruments, the Nobeyama Radio Heliograph (NoRH) at 17 and 34 GHz, and the Reuven Ramaty High Energy Solar Spectroscopic Imager (RHESSI). This flare is one of the few in which electromagnetic emission up to 300 – 800 keV has been observed and imaged up to energies exceeding 200 keV. In this paper, we will be concerned with the main phase of the flare which was observed well by both NoRH and RHESSI. We discuss the HXR and microwave spectra, the positions of the peaks relative to magnetograms, HXR positions relative to 17 GHz positions in both intensity and polarization. Finally we discuss the implications of high energy electrons in the context of the sunspot region where the flare occurred. Although the event all in all appears to correspond to the standard scenario with magnetic reconnection under an eruptive filament, several its features do not seem to be predictable by popular flare models. In particular we find that (1) microwave emissions might be optically thick at high frequencies with a low peak frequency of the total flux radio spectrum — due to the inhomogeneity of the emitting source, (2) magnetic fields in high-frequency radio sources might be stronger than sometimes assumed, (3) non-thermal electron spectra might have cutoffs at some hundreds keV mimicking some properties of thermal spectra, (4) significantly different properties of electron spectra of flare sources above similar sunspots. Our results emphasize the importance of studies of sunspot-associated flares and total flux measurements of radio bursts in the millimeter range.

Keywords: Flares, Impulsive Phase; X-Ray Bursts, Hard; Radio Bursts, Microwave (mm, cm)

[1]Astronomy Department, University of Maryland, College Park, MD 20742 email: kundu@astro.umd.edu email: ed@astro.umd.edu email: white@astro.umd.edu
[2]Lab for Astronomy and Solar Physics, NASA Goddard Space Flight Center, Greenbelt, MD 20771
[3]Institute of Solar-Terrestrial Physics, Irkutsk 664033, Russia email: grechnev@iszf.irk.ru

1. Introduction

Energetic electrons accelerated to energies of tens and hundreds keV can be observed through microwave and hard X-ray (HXR) emissions from the solar corona. Imaging observations are important to study the origin of energetic electrons in large flare events, which in turn can be used to test flare models and other related theoretical issues. Two dedicated solar imaging instruments are at present available – one in X-rays and gamma-rays by the Reuven Ramaty High Energy Solar Spectroscopic Imager (RHESSI, Lin *et al.*, 2002) and the other in microwaves by the Nobeyama Radioheliograph (NoRH, Nakajima *et al.*, 1994) at 17 and 34 GHz. NoRH is capable of imaging signatures of microwave emitting electrons in flaring sources. At 17 GHz it measures both Stokes I and V, and at 34 GHz Stokes I alone, with good sensitivity and spatial resolution of $\approx 10''$ and $\approx 5''$, respectively at the two frequencies. Signatures of hard X-ray emitting electrons are mapped by RHESSI.

RHESSI's primary objective is the study of energy release and particle acceleration in solar flares. This is accomplished by imaging spectroscopy of solar hard X-rays and gamma-rays over a 3 keV to 17 MeV energy range with energy resolution of ~ 1 keV, time resolution of ~ 4 s or better and spatial resolution as high as $2.3''$. For imaging, RHESSI uses a collimator-based Fourier-transform method. Rotational modulation by 9 fine to coarse fore- and aft grids provides amplitudes and phases similar to those used in radio interferometry. By means of a few methods, RHESSI produces maps in hard X-rays and gamma-rays.

Non-thermal microwave emission during large solar flares is produced by the gyrosynchrotron mechanism which involves coronal magnetic fields of at least a few hundred gauss and electrons of hundreds of keV and higher energy. Hard X-ray emission, on the other hand, is mainly produced by bremsstrahlung from precipitating electrons of a few to hundreds of keV energy. The two different methods of mapping energetic flare electrons therefore complement each other, and provide good means of testing flare-related concepts which have been abundant in the recent literature. One should herewith keep in mind general differences between the results provided by the two methods. The major hard X-ray flux is emitted by precipitating electrons striking a thick target, whereas microwaves are emitted by electrons gyrating in magnetic fields, both precipitating and trapped in coronal magnetic tubes. Therefore, microwave time profiles are often delayed and smoothed with respect to hard X-rays.

Next, the gyrosynchrotron emission is responsive to electrons with energies of hundreds keV and even a few MeV; by contrast, lower-energy electrons provide the major contribution to hard X-rays due to their excess in declining spectra. Furthermore, microwave and HXR emissions dominate at different ends of an asymmetric loop, because stronger magnetic fields suppress precipitation of electrons, but amplify the gyrosynchrotron emission.

Several issues related to accelerated electrons in solar flares are debated in the literature. First, it is not clear if a single acceleration mechanism operates in a flare or different mechanisms contribute (e.g., Wild, Smerd, and Weiss, 1963; Bogachev and Somov, 2001). Note that the possible presence of different "accelerators" does not necessary show up in the shape of the electron spectrum

(Bogachev and Somov, 2007). One cannot also rule out a possibility that in an event with repetitive acceleration/injection episodes some part of an electron population accelerated in the previous episode undergoes an additional acceleration from basically the same mechanism.

One more question is related to harder electron spectra inferred from microwave observations at frequencies believed to be optically thin with respect to those inferred from HXR data as initially shown by Kundu *et al.* (1994) and repeatedly confirmed afterwards. Following the interpretation of Melnikov and Magun (1999), other researchers (e.g., Silva, Wang, and Gary, 2000; Lee, Gary, and Shibasaki, 2000; Takasaki *et al.*, 2007) suggest to explain this fact by the collisional hardening of the electron spectra in magnetic traps.

Another possibility was proposed by White *et al.* (2003) who considered high-frequency radio emissions at 35 and 80 GHz in a major flare of 2002 July 23. From the analysis of the microwave/millimeter and HXR data they concluded that the trapping could not explain the difference between the electron indices inferred from these emissions in that event. They "were forced to assume that the 35 – 80 GHz spectrum did not represent optically thin emission"—even at such a high frequency as 35 GHz. They therefore concluded that the true optically thin radio spectral index was probably steeper. This possibility required a very large number of emitting electrons with a hard spectrum, which they indeed found in that event, up to 10^{10} cm^{-3} above 20 keV with a power-law index $\delta \approx 4.5 - 5$. The conclusion of White *et al.* (2003) suggests that a similar situation might occur in other events; with a lesser number of power-law electrons, the optically thick regime could reach high radio frequencies if magnetic fields are strong.

Here we discuss the RHESSI HXR and NoRH microwave imaging observations of the flare of 2003 June 17. The flare in question was of class M6.8, and it was observed in AR10386 (S08 E58), a $\beta\gamma\delta$-region, two days after its east-limb passage. This flare, unlike many others, produced a multitude of strong, isolated bursts seen in HXR and microwaves, combining a few similar events occurring at nearly the same place under similar conditions and promising important information on accelerated electrons. This flare was previously discussed by Ji, Huang, and Wang (2007) in the context of motions of flare loops. In our paper, we address high-energy emissions observed during this flare both in the microwave and hard X-ray domains and up to lower gamma-rays. Emissions exceeding 300 keV have been observed in very few flares, while 300 – 800 keV emission was well pronounced during one of peaks of the flare under discussion. Moreover, sources of such high-energy emissions have been mapped in still fewer number of flares, while the 2003 June 17 event gives such a chance.

We analyze a little known morphology of emission sources excited by electrons with energies up to hundreds keV. Then we consider the HXR and microwave spectra and images endeavoring to find out if they agree with each other or not and for what reasons. We concentrate on a peak of the event, during which the strongest emissions were observed at highest energies. It is also important to figure out conditions under which such strong events occur.

2. Observations

The event was well observed by RHESSI and other instruments such as the Transition Region and Coronal Explorer (TRACE, Handy *et al.*, , 1999) at 1600 and 195 Å. The Michelson Doppler Imager (MDI, Scherrer *et al.*, 1995) on SOHO has provided magnetograms and continuum images close to the event occurrence. Good RHESSI hard X-ray images are available from about 22:22 (all times hereafter are UT). The event was also observed in soft X-rays by GOES/SXI and in the Hα line in Big Bear (we do not use these images in our paper). The event started with a filament eruption observed in extreme ultraviolet (EUV) and Hα (Ji, Huang, and Wang, 2007).

The rise phase of the event occurred before NoRH started observing for the day, so radio images are only available from 22:45 onwards. In addition to NoRH, we also have data from total flux monitoring Nobeyama Radio Polarimeters (NoRP, Torii *et al.*, 1979; Nakajima *et al.*, 1985) at seven frequencies – 1, 2, 3.75, 9.4, 17, 35, and 80 GHz. The HXR and microwave light curves are shown in Figure 1. The impulsive rise in hard X-rays above 25 keV begins at 22:38, with steepest rise at 22:39, and the first HXR maximum in the 50 – 300 keV bands at about 22:40 (with several sub-peaks in the 25 – 50 keV range).

2.1. The Microwave and Hard X-ray Main Phase

In HXR time profiles in the main phase (Figure 1) we discern four distinct peaks 1, 2, 3, and 4. Peak 1 (22:39 – 22:43) is not observed in Nobeyama due to night time. The spatial structures observed during an enhancement labeled 2a (22:44:50 – 22:45:40) that passes into peak 2 differ from those observed during peak 2 itself, and therefore we consider it separately. Peak 2 (22:45:40 – 22:47:30), peak 3 (22:48 – 22:52), and peak 4 (22:53 – 22:57) are followed by a plateau in the HXR emission profile which we call the shoulder (22:57 – 23:00) discernible at 25 – 50, 50 – 100, and 100 – 300 keV. The hardest emission is mostly faint, becoming well pronounced only during peak 4. Note that HXR emission >300 keV is observed in only a handful of flares, and this flare is one of the few ever observed that shows HXR emission in the 300 – 800 keV band.

As mentioned earlier, because of the Nobeyama night time, NoRH and NoRP did not observe the early phases of this flare. We have examined the Palehua RSTN[1] radio time profiles, and they confirm that the true radio onset at microwaves was at 22:39. The radioheliograph and polarimeters at Nobeyama commenced observing at 22:45, starting with the rise of HXR peak 2a. All other peaks are observed by NoRP up to 80 GHz, including the shoulder at the end of peak 4. The microwave time profiles recorded in Nobeyama basically resemble the HXR records, but they are smoother, and their maxima lag behind the HXR peaks by several tens of seconds. This results in a larger overlap of peaks 2 and 3 with respect to hard X-rays. The shoulder is better pronounced in microwaves than in hard X-rays, even exceeding peak 4 at 35 and 80 GHz in intensity. The

[1] http://www.ngdc.noaa.gov/stp/SOLAR/ftpsolarradio.html

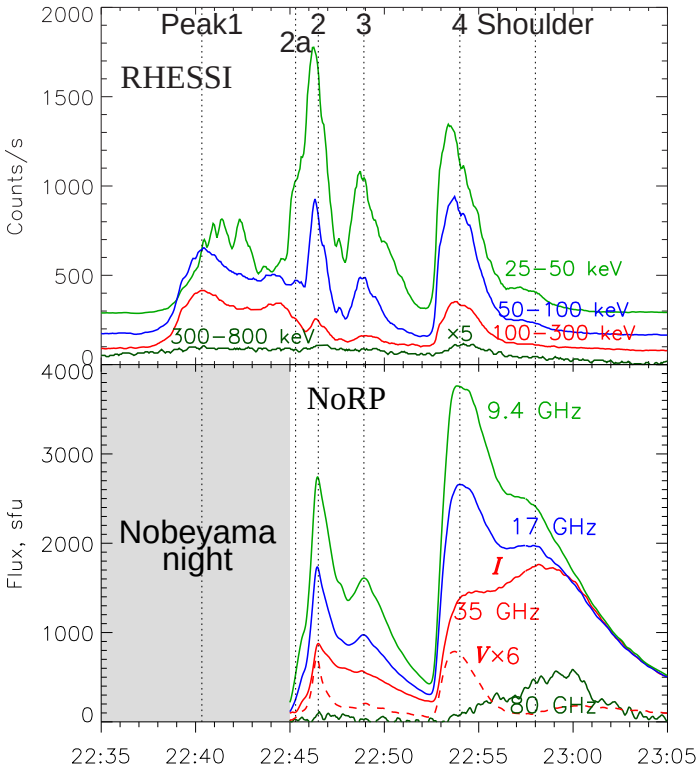

Figure 1. RHESSI hard X-ray (top) and NoRP microwave (bottom) total flux time profiles. The 300 – 800 keV band is magnified by a factor of 5. Prominent peaks as well as a later shoulder are denoted for convenience. RHESSI background levels are shifted to show the bursts better. Radio light curves are shown for Stokes I, and for Stokes V at 35 GHz only (dashed; magnified by a factor of 6).

microwave burst is very strong, reaching 3800 sfu at 9.4 GHz, 2600 sfu at 17 GHz, and 1700 sfu at 35 GHz. Also remarkable is the decay after 23:00, when the flux densities at 9.4, 17, and 35 GHz become almost the same.

A strong emission up to ∼ 600 sfu is also recorded at 80 GHz. Measurements of the flux density at 80 GHz from NoRP records are complicated by the following circumstances. A polarization switch of the 80 GHz radiometer degraded for several years, and the problem was fixed on 2005 June 23. Accordingly, the flux values at 80 GHz measured since 1999 June till 2005 June 23 gradually decreased with respect to their true values. To repair the 80 GHz flux density, a time-dependent correction factor was inferred from several calibrations (H. Nakajima, 2006, private communication):

$$k_{\rm cor}(80\,{\rm GHz}) = [T_{\{\rm Year\}}/1995.83]^{630}. \qquad (1)$$

The accuracy of the corrected total fluxes at 80 GHz within this time interval is considered to be ±40%, whereas polarization measurements should not be used. Data at 35 GHz and, especially, 80 GHz are affected by the atmospheric absorp-

tion. Uncertainties of the background level contribute to measurement errors. All these factors decrease the measurement accuracy at high radio frequencies.

The flux density at 9.4 GHz surpasses the fluxes at higher frequencies during all peaks, except for the shoulder. The excess of the 9.4 GHz emission is often considered as an indication that the peak frequency of the flaring microwave sources is < 17 GHz, and hence both 35 and 17 GHz emissions are believed to correspond to the optically thin regime. However, this indication could be misleading, as we show further.

The time profiles at lower frequencies of 1, 2, and 3.75 GHz, which are not shown in Figure 1, mainly correspond to the time profile at 9.4 GHz. The resemblance of the time profiles in the whole range of 1 – 80 GHz suggests the dominance of the same emission mechanism in this range. The only exception is subsidiary spiky structures of $\lesssim 20\%$ visible at 1 GHz on top of the smoother background, probably due to a contribution from plasma emission mechanism.

2.2. The Flare Configuration

2.2.1. Flare Ribbons and HXR Sources

This flare occurred in a region which in white light (WL) consisted of a complex of sunspots with strong umbrae and penumbrae. The Hα flare was entirely observed in Big Bear Solar Observatory. However, we mainly use in this paper two TRACE 1600 Å images, because the latter ones do not suffer from atmospheric effects unlike ground-based Hα observations. The TRACE 1600 Å channel is sensitive to emissions from 4 000 – 10 000 K plasmas; hence bright features in 1600 Å images basically correspond to structures visible in Hα.

The TRACE absolute pointing coordinates have an uncertainty significantly larger than its spatial resolution of $1''$[2], whereas those of RHESSI are more accurate. For this reason, coordinates in all figures are referred to RHESSI pointing. To co-align the TRACE and RHESSI images, we compared the TRACE WL images with full-disk MDI ones. In this way, the solar rotation was compensated through a re-projection of the continuum images to the same time (analogous routines were performed with MDI magnetograms). Residual inaccuracies of a few arc seconds are possible.

Figure 2 outlines the flare configuration. The TRACE 1600 Å images show the flare ribbons at peak 3 (a) and late in the decay phase (c). Their contours are also overlayed on top of TRACE WL images observed at nearly the same times (e, f). The RHESSI 12 – 25 keV and 50 – 100 keV images observed at peak 3 are presented in panel (d), and the contours of the same 50 – 100 keV images are shown on top of the TRACE WL image (e). Panel (f) shows the TRACE WL decay-phase image as grayscale background along with flare ribbons and oval black/white dashed contours of the RHESSI 100 – 200 keV images observed at peak 4.

[2]see http://trace.lmsal.com/Project/Instrument/cal/pointing.html and http://trace.lmsal.com/tag/

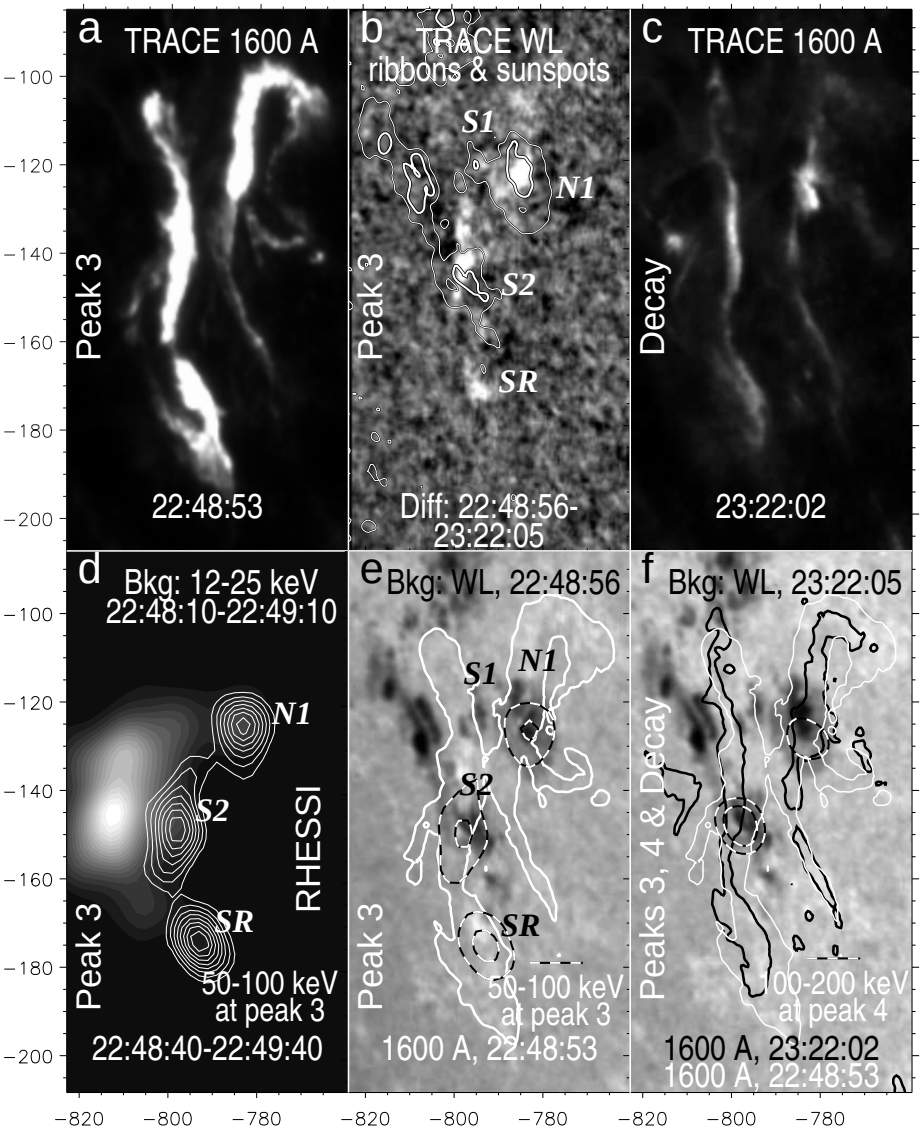

Figure 2. Flare ribbons, HXR sources, and sunspots. Ribbons were observed by TRACE during peak 3 (a, b, e) and late in the decay phase (c, f) in the 1600 Å images (a, c) and WL ones (b, e, f). Panel (b) shows a WL difference image with contours of the sunspot umbrae and penumbrae. The lower row also shows HXR RHESSI images at peak 3 (d, e; 50 – 100 keV) and peak 4 (f; 100 – 200 keV). Levels of dashed contours in panels (e, f) are 40% and 80% of the maximum. White contours in panel (e) and black ones in panel (f) correspond to the closest 1600 Å images, white contours in panel (f) reproduce the ribbons shown in panels (a, e). "N1", "S1", and "S2" denote major sunspots related to the flare site according to their polarities, and "SR" denotes the southern region of the flare. Axes show hereafter arc seconds from the solar disk center according to the pointing of RHESSI and MDI.

Although the configuration looks like a two-ribbon flare (Ji, Huang, and Wang, 2007), the situation is not quite a typical one. Unlike an ordinary flare, the ribbons in this event cross sunspots (N1 and S2) almost covering them, even including their umbrae. The emission of the ribbons is faintly visible along the axes of the ribbons in the background WL image in Figure 2e to cross sunspots N1 and S2 and near the southern region SR. Panel (b) presents a WL difference image, in which these brightenings are clearly visible. They are most likely due to the leakage of UV emissions in the TRACE wide-band continuum channel; besides, a white-light flaring is also possible (*cf.* Metcalf *et al.*, 2003; Hudson, Wolfson, and Metcalf, 2006). The HXR sources are also located within sunspots (N1 and S2), overlapping with their umbrae. Besides the main sources associated with sunspots N1 and S2, there is an additional flare source south of S2 denoted "SR".

2.2.2. Overall Story of the Event

Having revealed the flare configuration and its main particularities, now we consider the development of the event from its start up to the late decay. Coronal phenomena are shown by TRACE 195 Å images in Figure 3a – e as well as an Hα image in panel (f). A more detailed information is presented by a movie RHESSI_TRACE.mpeg accompanying the electronic version of our paper, which shows a movie composed of the TRACE 195 Å images overlayed with RHESSI 12 – 25 keV (red) and 50 – 100 keV (green) contours.

A system of filaments (F1, F2, F3) covered the whole pre-event region with their northern ends being rooted approximately between N1 and S1 and the southern ends somewhere near SR. At least, one of filaments (F1) activates at about 22:23, which is manifest in its brightening, and starts to gradually rise (Figure 3a). The activation probably also involves filament F2. This time corresponds to the earliest detectable increase of the soft X-ray flux recorded with GOES monitors (the onset of the event in soft X-rays was reported to be at 22:27). The brightening of the filament indicates its heating up to coronal temperatures, while RHESSI shows the presence of still hotter plasmas in this region. The coronal X-ray source detectable up to 25 keV is arranged along the brightening filament.

Then the filaments unbend and rise to take a vertical position, while their southern ends remain fixed in the position close to the future southern flare region SR (Figure 3b). When the northern ends of the filaments reach a significant height, the HXR flux also starts to increase. Figure 3c shows the last 195 Å image (at 22:39:25), in which the filaments are discernible; in the next 195 Å image (22:40:40), they disappear most likely due to a rapid eruption. Note that the first HXR peak occurs just at this time.

The flare sources N1 and SR are obviously associated with the positions of ends of pre-eruptive filaments. The region SR is located just below the fixed end of the rising filament.

The TRACE 195 Å images obtained at peaks 3 and 4 (Figure 3d, e) show a typical arcade of flare loops arranged along the former position of the erupted filaments. The arcade does not exhibit any conspicuous particularities. Noticeable are bright kernels in its base which coincide or almost coincide with HXR

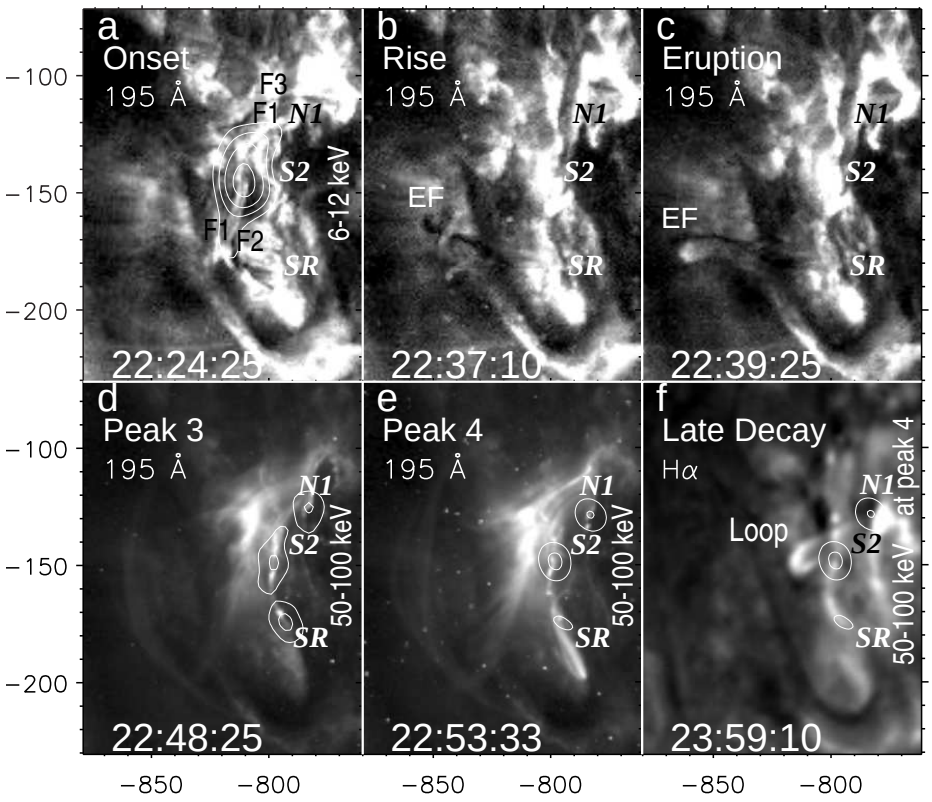

Figure 3. Coronal images of the event from the onset up to its late decay: (a): activation of filaments, (b, c): their rise and eruption, (d, e): peaks 3 and 4, (f): late decay. Grayscale background shows TRACE 195 Å images in panels (a – e) and a BBSO Hα images in panel (f). Contours show RHESSI images. Labels "N1", "S2", "SR" denote flare regions. Filaments visible in TRACE images are labeled "F1 – F3" in panel (a) and "EF" in panels (b, c) showing their eruption. A late-stage Hα image (f) shows a post-flare loop between N1 and S2.

sources. Hα images obtained late in the decay phase of the event sequentially show cooling post-flare loops. Remarkable is a loop between N1 and S2 caught in an image shown in Figure 3f (the outer edge of its northern leg is already getting dark, while the whole loop remains semi-transparent).

2.2.3. Hard X-Ray Morphology

In hard X-rays, the time profile of the flare shows the usual gradual behavior below 25 keV and multiple impulsive spikes at higher energies. The images in the lower energy bands for 6 – 12 and 12 – 25 keV, most of which we do not present, show that the flaring region consists of, with a few exceptions (22:52:40 – 22:55:00), compact sources with apparent flux maxima at $\sim$ 22:46 – 22:51 and 22:54 – 22:55. The gradual profile continues until the end of RHESSI sunlight at 23:06. At these low energies, except from 22:52 to 22:55, one does not see foot points — only a loop-like structure. In the higher energy channels, 25 – 50 and

50 – 100 keV, right from the beginning the main flaring region is resolved into two or more individual sources.

The HXR count rate profiles at 25 – 50 and 50 – 100 keV of the impulsive phase show four peaks labeled 1, 2, 3, and 4 in Figure 1. Each of these has a different morphology, spectrum, and temporal behavior. To obtain a coherent perspective, we studied the morphology and spectra for each of these. In each case we overlaid the HXR sources on an MDI magnetogram made at the start of the flare. The main result that comes out of this morphological studies is that at lower energies one sees the entire flaring loops, including in some cases the loop tops. At higher energies one sees the footpoint regions beautifully. This is especially true for peaks 2, 3, and 4. An example is shown in Figure 2d for peak 3. Figure 7a also shows the same morphology with higher energy channels at 100 – 200 and 200 – 400 keV bands included. This may be one of the few events where we have been able to map such high energy electron bremsstrahlung sources. Note that there is no dispersion in source position (to $< 1''$) as a function of energy over the entire range 25 – 400 keV at the onset of peak 4.

2.2.4. Radio Sources

Our observing with NoRH started in the morning hours when the beam was strongly elliptical. We therefore used other techniques to have better spatial resolution. The NoRH images at 17 and 34 GHz were synthesized from raw data files by means of the NRAO AIPS package using uniform weighting of visibilities. The ultimate resolution was of order $12''$ at 17 GHz and $8''$ at 34 GHz. The final calibration of the brightness temperatures in the images was performed by referring to the NoRP total flux records.

The co-alignment of microwave sources with other images is not a simple task. The coordinates of the NoRH images are generally found by referring to the position of the quiet solar disk. Therefore, when the uncertainties of computations of the solar disk's position are large, the positional accuracy of the NoRH images is poor. They can also suffer from relative shifts. The accuracy of the co-alignment can be improved by referring to some features in other images, e.g., by comparing the radio polarization with a magnetogram. Microwave flare emissions are usually dominated by gyrosynchrotron from power-law electrons, which can be significantly polarized in the sense of the x-mode emission at optically thin frequencies. Thus, the sign of the radio polarization coincides in this case with the polarity of the magnetic field. At frequencies below the turnover of the spectrum, where the emission is optically thick, the radio polarization significantly decreases, and its sign changes to the o-mode one. Taking account of these circumstances, we co-aligned the NoRH 17 GHz maps with the magnetogram and HXR images. The residual inaccuracy might exceed a few arc seconds. The NoRH images at 17 GHz are shown in Figure 4 in the left column (Stokes I) on top of the TRACE WL image and in the middle column (Stokes I and V) on top of the pre-event MDI magnetogram.

The accurate co-alignment of the 34 GHz images is still more problematic. NoRH does not provide images of the polarized component at 34 GHz. To find the correct positions of the 34 GHz sources, one has to compare their shapes with

Figure 4. Flare morphology observed during peaks 2a – 4 and shoulder (consecutive rows). *Left column*: overlays of 17 GHz (black) and 34 GHz (white) contour maps on a TRACE WL image observed at 23:22:02. *Middle column*: 17 GHz Stokes V maps (white; solid positive, broken negative) and Stokes I maps (black) on an MDI magnetogram observed at 22:23 (bright N, dark S). *Right column*: RHESSI 50 – 100 keV (black) and 35 GHz contour maps on the same TRACE WL image as in the left column.

those at 17 GHz or HXR. Involvement of other information or considerations is sometimes required, but all these ways do not guarantee a successful outcome. The 34 GHz images are shown in Figure 4 in the left and right columns. Their positions at peak 4 and the shoulder (two lower rows) do not cause questions. However, the absence of the 34 GHz emission from the region of the strongest 17 GHz emission in N1 in three upper rows appears to be surprising and doubtful. Nevertheless, after a careful analysis of all the sources at both 17 and 34 GHz as well as HXR sources we are confident that their co-alignment is correct to a few arc seconds. Besides the resemblance of the shapes visible in Figure 4, our confidence is based on the analysis of all 301 sets of radio images produced for the whole event with an interval of 4 s, gradual changes of their shapes, and evaluation of the significance of side lobes of the NoRH beam as well.

Figure 4 shows microwave sources at 17 and 34 GHz (NoRH) and RHESSI 50 – 100 keV images on top of the decay-phase TRACE image (left and right columns) and an MDI magnetogram (middle column). The maximum brightness temperatures over the images are shown in Figure 5 (for 17 GHz in the top row and for 34 GHz in the bottom row). The areas of the microwave sources measured at peak 4 are as follows. The areas of the main 17 GHz sources are 207 arcsec^2 (1.1×10^{18} cm^2) in sunspot N1 and 162 arcsec^2 (8.8×10^{17} cm^2) in sunspot S2; the areas of the 34 GHz sources are 36 arcsec^2 (2×10^{17} cm^2) in sunspot N1 and 108 arcsec^2 (5.9×10^{17} cm^2) in sunspot S2.

Starting from the onset of observations in Nobeyama, the 17 GHz emission is dominated by sunspot N1; some contribution from S1 and S2 is also detectable. A similar picture is shown by hard X-rays. In addition, there is a detectable HXR emission from the southern region SR. Unlike the 17 GHz emission, the 34 GHz sources are concentrated in sunspot S2 and SR. From the enhancement 2a to peak 2 and then to peak 3, the source above sunspot S2 increases its importance, while the HXR emission in S1 relatively decreases. At peak 4 and later on, sunspot S2 dominates, and the strongest emissions come from its umbra, while the sources in sunspot N1 shift south, into its penumbra. During the shoulder, the main source of all emissions is located in S2.

The southernmost flare source denoted "SR" is well pronounced in hard X-rays, but weak at 17 GHz, obviously due to significantly weaker magnetic fields in this region (the microwave intensity is determined by a rather high power of the magnetic field strength). Unlike the sources above sunspots N1 and S2, the source in SR is localized above a bipolar magnetic region. The magnetic field strength in this region varies from −770 G to +900 G under the HXR source.

The magnetic field strengths on the photosphere were measured from full-disk MDI magnetograms. Note that the MDI magnetograms were recalibrated late in 2007, which resulted in an increase of the magnetic field strengths by a factor of about 1.7 (see http://soi.stanford.edu). In addition, the position of the active region far from the solar disk center (S08 E58) causes a projectional reduction of the magnetic field strength. Its correction is generally questionable, because the direction of the magnetic field vector might be different. However, we are dealing with main flare sources associated with sunspots, where the magnetic field is nearly radial, and a radialization correction appears to be justified. We have made it using the *zradialize* SolarSoftware routine. The radialization factor

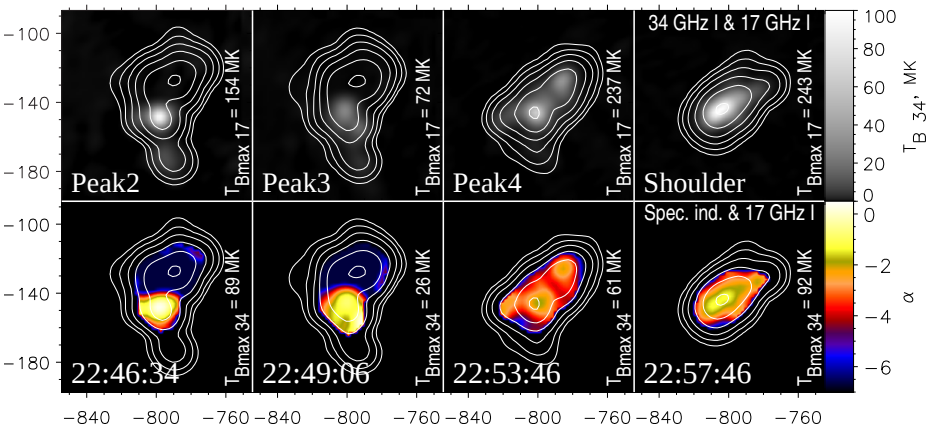

Figure 5. Microwave images and spectral indices. 34 GHz images (top row) and spectral indices (bottom row) both overlaid by contours of 17 GHz images. Contour levels in each image are at 0.9 of its maximum divided by powers of 3. Scale bars on the right quantify the grayscale and color representations. The maximum brightness temperatures over each image are specified in the upper row for 17 GHz and in the lower row for 34 GHz.

is from 1.82 in N1 up to 1.93 in S2. The maximum magnetic field strength measured from the projection-corrected magnetograms is +3080 G and −2120 G in sunspots N1 and S2 associated with major microwave sources, respectively. The maximum strength in sunspot S1 is −1750 G.

The microwave polarization is of a special interest. It shows a beautiful picture which mainly corresponds to the magnetogram. The degree of polarization in N1 initially reaches 50% at peak 2a, and then mostly persists at a level of about 30%. The degree of polarization in S2 is 20 – 30% throughout the event. However, the contours of the polarization do not perfectly correspond to the magnetic polarity everywhere. The most conspicuous are discrepancies at peak 2a – 2 in the region of the main source (N1) and both north and south of it. The polarization structure vigorously varies at this time. Similarly, discrepancies are observed at peak 4 and the shoulder northeast and southwest of S2. It is not possible to explain the discrepancies between the microwave polarization and the magnetogram by insufficient spatial resolution only; changes from the x-mode to the o-mode emission are undoubted. This fact hints at a possibility that the 17 GHz emission might not be optically thin.

To check for this possibility, we show in Figure 5 the 17 and 34 GHz Stokes I images (top row) and a microwave spectral index computed from the spatial distributions of the brightness temperatures at these frequencies (bottom row). The hardest optically thin microwave index α_T is −3.5 for the hardest realistic power-law index of the electron number spectrum $\delta = 3$ ($\alpha_T = 1.22 - 0.9\delta - 2$, Dulk and Marsh, 1982). As we will see below from HXR spectra, in this event $\delta \approx 4$, and $\alpha_T \approx -4.4$. Thus, orange, brown, and yellow regions are certainly optically thick at 17 GHz; moreover, it is possible that blue regions only are optically thin.

A movie overlay_wl_17.gif accompanying the electronic version of our paper shows the radio blob superimposed on the sunspot complex. The main point

here is that the flaring source at 17 GHz covers the sunspot umbrae considerably. This is one of the important characteristics of this flare, and it is possible that this particular characteristic contributes to the very high energy electron bremsstrahlung (up to 800 keV) that we have observed in this flare.

From this morphological study one sees that strong X-ray and microwave flare emissions are radiated by a few loops, some of which are rooted in sunspots. A loop between N1 and S1 is detectable during peaks 2 and 3 and, especially, enhancement 2a before them. The southern region SR probably also has a loop structure and is connected with N1. Emissions during peak 4 and the shoulder are dominated by a loop between N1 and S2. Both the microwave and HXR sources have similar structures at this time. The most important point to note here is that the flaring source during peak 4 occurs just above sunspot umbrae. While footpoints mainly radiate at 34 GHz and in HXR, emissions of the whole loops are also detectable at 17 GHz. A quasi-periodic character of the whole event might be due to sequential involvement in the flare of a few major flare loops.

2.3. Spectral Data

Computations of HXR spectra are complicated by several changes of the RHESSI attenuator and decimation states. The attenuator of the front detectors shifted at about 22:32:30 and had not reverted to its previous state until the end of the flare (the operation modes of the rear detectors also changed). The background level becomes therefore questionable, and a straightforward way to get mean spectra would be unreliable. For this reason, we had to use computations of the spectra from imaging data. This way allows one to get the spectral information for each HXR-emitting source individually, and it also appears to effectively suppress the contribution from the photospheric albedo.

The Clean method does not seem to produce well-calibrated results when the state of the attenuator changes. We compared results obtained by means of the Pixon and Forward Fit methods. After some tests we have found both of them to produce similar satisfactory results, and mainly used afterwards the Forward Fit, which consumes much less time than the Pixon method. To get correct results with the Forward Fit, we took information about the number and shapes of the emitting sources from HXR images produced using the Clean method, and sometimes the Pixon method for each instant analyzed. Since the non-thermal part of the spectra is of our major interest, we mostly consider them above 30 keV.

2.3.1. HXR Spectra at Peak 2

Peak 2 is of a special interest, because at this peak we have encountered a puzzling situation with no 34 GHz emission from the region of the main 17 GHz source. Such a situation is possible when dealing with a thermal gyroresonance emission at low harmonics of the gyrofrequency. HXR spectra of the three main sources N1, S2, and SR are shown in Figure 6.

The spectra of the three sources are significantly different at peak 2. The source above sunspot S2 has a hardest spectrum with $\gamma = 2.8$. The spectra of

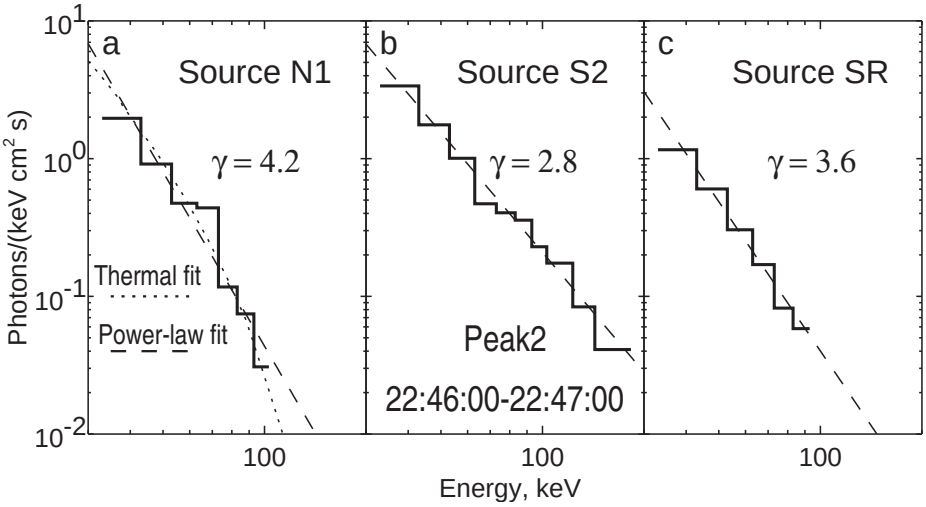

Figure 6. Spatially-resolved hard X-ray spectrum observed with RHESSI during peak 2. Panels a, b, and c show the spectra of different HXR sources (histograms) along with a power-law fit (dashed lines). The spectrum of the source associated with the N1 sunspot (a) is additionally fitted with a thermal continuum spectrum (dotted line).

the two other sources are significantly softer ($\gamma = 4.2$ and 3.6) and could not be reliably constructed above 100 keV. Note that the source above S2 is the hardest one throughout the flare (whereas we do not know about peak 1).

The spectrum of the source above sunspot N1 can be successfully fitted with either a power-law (dashed line in Figure 6a, $\gamma = 4.2$) or a thermal continuum without emission lines (dotted line); $\chi^2 < 1$ in both cases. For the thermal fit, the temperature is 230 MK, and emission measure is 3×10^{-53} cm^{-3}. Such a huge temperature does not seem to be realistic; we discuss this issue below.

2.3.2. HXR Images and Spectra at Peak 4

Figure 7a shows images in energy bands from 25 to 400 keV produced using the Pixon method within the interval of 22:52:40 – 22:54:30. There is no dispersion in source position (to $< 1''$) as a function of energy at 22:52:40, and then the northern source displaces. The middle source S2 remains stable.

Figure 7b shows a spectrum produced from RHESSI observations during peak 4. The low-energy part of the spectrum was constructed using front detectors, and the 300 – 800 keV part marked by filled circles was constructed using rear detectors. To enhance the sensitivity, we computed the spectra using all three HXR sources. Due to a relatively poor count rate at high energies and other complications we have not succeeded in a perfect concatenation of the parts constructed with different detectors; nevertheless, the overall slopes below and above 300 keV appear to be the same.

To summarize the power-law electron number spectral index δ inferred from the power-law indices of HXR spectra γ ($\delta = \gamma + 1.5$) is hardest in the source above sunspot S2 during all peaks, slightly hardening from 4.3 at peak 2 to 3.8

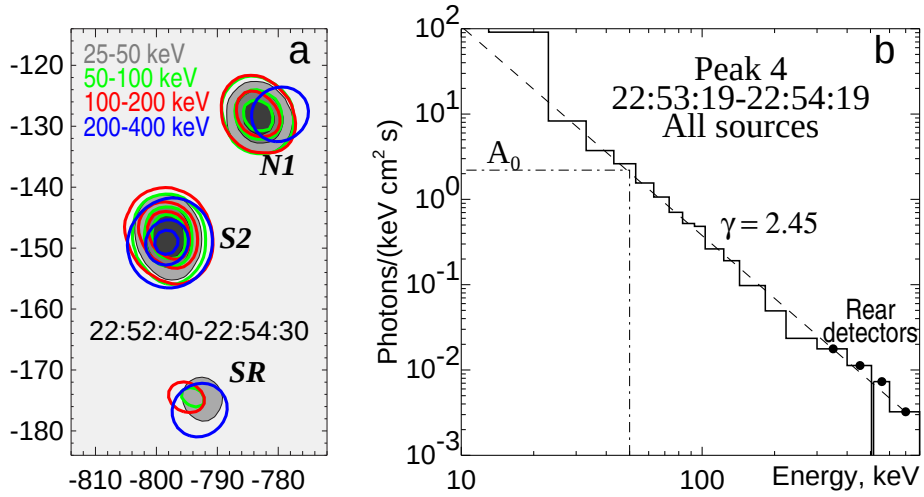

Figure 7. Peak 4 in hard emissions. (a) Images in energy energy bands from 25 to 400 keV. Contour levels are 15%, 50%, and 80% of the maximum. (b) Hard X-ray and gamma-ray spectrum observed with RHESSI during peak 4 (histogram) along with a power-law fit (dashed line) of the part >30 keV with $\gamma = 2.45$, $A_{0\,(50\,\mathrm{keV})} = 2.2$. The 300 – 800 keV part (marked by filled circles) was constructed using rear detectors, while front those were used for lower energies. A probable nuclear 511 keV line was preventively rejected.

at the shoulder. The spectrum in N1 is initially very soft, $\delta \approx 5.7$ at peaks 2 and 3, and then it becomes about 4.2 and persists later on. The source SR is well detectable during peaks 2 ($\delta \approx 5.1$) and 3 ($\delta \approx 6$) and fades out during peak 4.

2.3.3. Microwave Spectra

Figure 8 shows the microwave spectra at four different epochs — peaks 2, 3, 4, and the shoulder, using the NoRP frequencies at 1.0, 2.0, 3.75, 9.4, 17, 35, and 80 GHz. All spectra show distinct maximum at about 10 GHz with the exception of the shoulder which seems to have a complex spectrum, with two peaks: $\nu_{\mathrm{peak\,1}} \approx 10$ GHz, $\nu_{\mathrm{peak\,2}} > 20$ GHz. The thick dotted lines in all panels show the highest-frequency slope $\alpha = 1.22 - 0.9\,\delta_{\mathrm{RHESSI}}$ corresponding to the RHESSI spectrum of the hardest HXR source S2, which should dominate the highest-energy hard X-rays as well as the highest-frequency radio emissions.

The shapes of the spectra imply non-thermal emission for all four epochs shown in the figure. Recalling that the microwave flux densities become almost the same during the decay (see Figure 1), it is useful to compare their values with estimates from soft X-ray observations.

From RHESSI 6 – 12 keV images at 22:53 – 22:57 we find an SXR-emitting area to be $A \approx (2-6)\times 10^{18}$ cm^2 (levels of 0.3 – 0.6 of the maximum), and a volume $\sim A^{3/2} \approx (4-13)\times 10^{27}$ cm^3. From RHESSI spectrum at 22:58 we find an emission measure of 2.8×10^{49} cm^{-3} and a temperature of 20 MK. For comparison, we estimated the temperature and emission measure variations throughout the event from GOES-12 soft X-ray fluxes using a recent GOES software with updated coronal abundancies (White, Thomas, and Schwartz, 2005). At the same time of

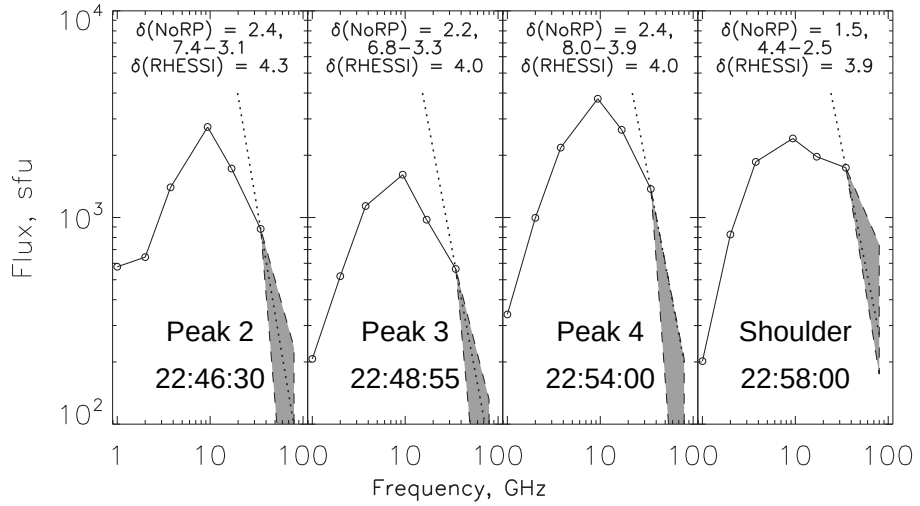

Figure 8. Microwave spectra. Shadings show the uncertainties of the flux density at 80 GHz. The spectral indices $\delta_{\rm NoRP}$ specified in panels a – d were calculated from the flux ratios at 17 and 35 GHz (upper row) as well as from the flux ratios at 35 and 80 GHz at the lower and upper boundaries of the shaded regions, respectively. The thick dotted lines show the highest-frequency slope corresponding to the RHESSI HXR spectrum.

22:58, these estimates provide an emission measure of 3.5×10^{49} cm^{-3}, density of $(5 - 10) \times 10^{10}$ cm^{-3}, and temperature of 15 MK — reasonably close to the estimates from RHESSI data. The thermal radio flux estimated from SXR data is maximum at 22:58 and does not exceed 28 sfu. Thus, non-thermal emissions appear to dominate all the microwave/millimeter sources throughout the event.

The slopes of the microwave spectra at the highest frequencies of 35 and 80 GHz appear to agree with electron spectrum power-law indices inferred from HXR data. The slopes between 17 and 35 GHz are significantly flatter than the spectra of the HXR-emitting electrons, with a difference of 1.6 – 1.9 and even up to 2.4 during the shoulder. This fact is consistent with our preliminary assumption that the 17 GHz emission is not optically thin, although the peak frequency of the microwave total flux spectrum is at about 10 GHz for the most part of the event.

2.4. Evolution of the Active Region

Now, when the main features of the event have been revealed and some important parameters are known, for the completeness of the picture we will follow the preparation of the event from the history of the active region. Figure 9 shows its evolution as observed by SOHO/MDI in magnetograms (upper row) and continuum images (lower row). The rightmost panels in both rows (e, j) show negatives of variance maps (see Grechnev, 2003), in which darkest patches represent regions which underwent most significant changes. The intervals of the variance analysis are indicated in variance maps. Gray contours of 50 – 100 keV images observed with RHESSI at peak 4 are also overlayed on the variance maps.

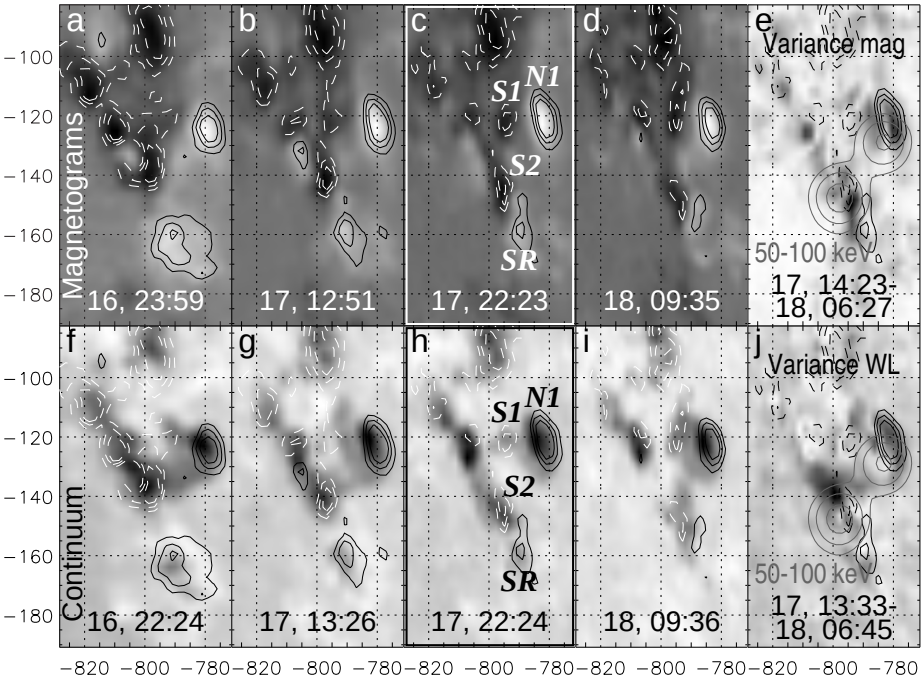

Figure 9. Evolution of active region 10386 as shown by MDI magnetograms (top row) and continuum images (bottom row). Black solid and white dashed contours correspond to the magnetic N and S polarities, respectively (levels are $\pm 500, 1000, 1500$ G). Right column (e,j) shows the negatives of the variance maps overlayed additionally with gray contours of 50 – 100 keV RHESSI images at peak 4. Panels c,h (in frames) correspond to the event occurrence. Labels denote the major flare sources. Days and times of the images are specified in each panel.

All the images are re-projected through a compensation of the solar rotation to the event occurrence. The images which are closest to the event (framed) are shown in the middle rows (c, h) and supplied with labels of the major flare sources.

During about 35 hr presented in the figure, the active region rapidly evolved. The S-polarity sunspot S2 significantly displaced southwest, towards the N-polarity northern part of the southern region SR. Another S-polarity region S1 formed near the largest sunspot N1. The magnetic field strength in S1 increased, but this region had not become a well-defined sunspot. As the variance maps computed both from magnetograms and WL images show, the flare sources N1 and S2 were located at the places where the main changes occurred on the photosphere. The rapid evolution of regions S2 and S1 probably prepared conditions for the event occurrence.

The maximum visible extent of N1 is $23''$(17 Mm). Estimating the field strength above an isolated sunspot with a radius b on its axis at a bottom of the corona (at a height $h = 3 - 4$ Mm) as $H_{\rm A}(h) = H_{\rm A}(0)(1 - h/\sqrt{h^2 + b^2})$ (e.g., Zheleznyakov, 1969), we get the strengths of 1500 – 1800 G above N1 and 820 – 1000 G above S2 (see Section 2.2.4). The magnetic fields above such an active region with a tight mixture of different polarities can be somewhat stronger.

However, the absence of stable gyroresonance sources in this active region before and after the event suggests that the magnetic field strength in the corona did not reach the third harmonic of the gyrofrequency at 17 GHz, i.e., $H < 2000$ G.

3. Discussion

3.1. Microwave/Millimeter Emissions

To compare the microwave parameters with parameters inferred from HXR spectra, we use a set of formulas compiled by White (2009). The photon spectrum of the non-thermal bremsstrahlung (or its parts in a few energy ranges) observed at energies exceeding the thermal domain is usually close to a power law:

$$\Phi(E_\gamma) = A_0 \left(\frac{E_\gamma}{E_0}\right)^{-\gamma} \text{ [photons keV}^{-1}\text{ cm}^{-2}\text{ s}^{-1}\text{]} \tag{2}$$

where E_γ is the photon energy, γ is the power-law index of the photon spectrum, and A0 is the normalization constant at a fiducial photon energy E_0 keV.

In the case of the RHESSI software, $E_0 = 50$ keV for the broken power-law fit to the spectrum, and the normalization obtained from the fit refers to this energy. As Hudson, Canfield, and Kane (1978) based on the theory of Brown (1971) showed, with a measured HXR photon spectrum (2), the corresponding electron flux spectrum into the thick target is given by

$$\frac{d^2N(E)}{dEdt} = 3.28 \times 10^{33} \frac{A_0 b(\gamma)}{E_{0\,[\text{keV}]}} \left(\frac{E}{E_0}\right)^{-(\gamma+1)} \text{ [electrons keV}^{-1}\text{ s}^{-1}\text{]}, \tag{3}$$

where $b(\gamma) = \gamma^2(\gamma-1)^2 B(\gamma - 0.5,\ 1.5)$ and $B(x, y)$ is the beta function. The $N(E)$ is the total number of electrons at energy E in some unspecified volume, and the expression in the left part of equation (3) represents the differential energy spectrum of its temporal variation.

The microwave flux density and its spectrum are determined by the number of electrons gyrating in the volume of a microwave-emitting source. From a relation between a density and a flux and assuming the downwards component of motion to carry one-third of the electron energy, it is possible to obtain the differential electron number spectrum in the non-relativistic approximation:

$$\frac{d^2N(E)}{dEdV} = 3.04 \times 10^{24} \frac{A_0 b(\gamma)}{E^{1.5}_{0\,[\text{keV}]} A_X} \left(\frac{E}{E_0}\right)^{-(\gamma+1.5)} \text{ [electrons keV}^{-1}\text{ cm}^{-3}\text{]}, \tag{4}$$

where the power-law index of the electron number spectrum δ is related to the power-law index of the thick-target photon spectrum γ as $\delta = \gamma + 1/2$ (Hudson, Canfield, and Kane, 1978).

The power in accelerated electrons above an energy E_1 striking the thick target is, from (3),

$$\int_{E_1}^{\infty} \frac{d^2N(E)}{dEdt} E dE = 5.25 \times 10^{24} \frac{A_0 b(\gamma) E_{0\,[\text{keV}]}}{\gamma - 1} \left(\frac{E_1}{E_0}\right)^{-\gamma+1} \text{ [ergs s}^{-1}\text{]} \tag{5}$$

To relate the parameters of electrons found from the photon HXR spectrum with the microwave emissions, simplified analytic expressions of Dulk and Marsh (1982) can be used. These expressions operate with a number density of electrons, N_r, in the distribution above the fiducial electron energy E_r, taken to be 10 keV

$$\frac{d^2N(E)}{dEdV} = N_r \frac{\delta - 1}{E_r} \left(\frac{E}{E_r} \right)^{-\delta} \tag{6}$$

From (4) and (6) one obtains

$$N_r = 3.04 \times 10^{24} \frac{A_0 b(\gamma)}{(\delta - 1) E_{0\,[\mathrm{keV}]}^{0.5} A_X} \left(\frac{E_0}{E_r} \right)^{\delta - 1} [\text{electrons cm}^{-3}] \tag{7}$$

The power-law index of the microwave total flux spectrum in the optically thin limit, α, is related to the power-law index of the electron number spectrum as $\alpha = 1.22 - 0.9\,\delta$ (Dulk and Marsh, 1982). Now it is possible to quantitatively compare the observed photon HXR spectra and microwave ones.

3.1.1. Emissions from N1 during Peak 2

As mentioned, the absence of emission at 34 in the source above sunspot N1 during Peak 2 (and 3) might be possible, if the 17 GHz emission is due to a thermal gyroresonance source. As Figure 6a shows, the HXR spectrum in source N1 is detectable up to about 100 keV and could be interpreted as a thermal one with a temperature of 230 MK or a power-law one with $\gamma = 4.2$.

Estimations of the non-thermal gyrosynchrotron emission from power-law electrons with $\delta = \gamma + 1.5 = 5.7$ using formulas of Dulk and Marsh (1982) show that the observed 17 GHz emission above N1 (150 MK) is possible. The ratio of the brightness temperatures at 34 and 17 GHz is $T_{34}/T_{17} \approx (34/17)^{(1.22-0.9\delta-2)} \approx$ 0.017, and the brightness temperature expected at 34 GHz in N1 should be about 2.5 MK even with such a soft electron spectrum. The maximum brightness temperature observed at 34 GHz at peak 2 is about 90 MK in S2; the dynamic range should be sufficient to detect a 2.5 MK source (3%, or −16 dB). It is not clear why the 34 GHz emission is absent in N1, if the emission is non-thermal.

Estimations of the gyroresonance emission using formulas from Zheleznyakov (1969) or White and Kundu (1997) show that with a temperature of 230 MK, not only the x-mode, but the o-mode also become opaque at a rather small viewing angle (30° for the fourth harmonic, 1520 G and 35° for the fifth harmonic, 1215 G). However, the radial direction of the magnetic field above sunspot N1 with a position of the active region on the Sun implies a viewing angle of ≈ 60° — in this case, the brightness temperature at 17 GHz would be 230 MK, and the southwestern edge of N1 only would be polarized. On the other hand, no other indications of such a huge temperature are present.

A probable solution of this problem is a non-thermal spectrum, which is power-law-like below 100 keV and has an upper cutoff at a somewhat higher energy. Such a spectrum has nothing to do with a thermal equilibrium, but mimics some of its properties. The number of moderate-energy electrons is sufficient to

produce the observed strong 17 GHz emission — even a thermal spectrum would suffice. However, the deficiency of higher-energy electrons probably determines the absence of the 34 GHz emission.

3.1.2. Emissions during Peak 4

Having parameters of the HXR spectra, one can estimate parameters of the radio emission. Calculations of radiation of electrons gyrating in magnetic fields (e.g., Ramaty, 1969; Ramaty *et al.*, 1994; Preka-Papadema and Alissandrakis, 1992; Bastian, Benz, and Gary, 1998) appears to be the most rigorous way. Another way introduced by Dulk and Marsh (1982) uses formal analytic approximations of the rigorous results. The common problem of both ways is due to large uncertainties of several important parameters; however, the latter way appears to be more flexible, it is not time-consuming, and allows to get tendencies easily.

First, we try to estimate the magnetic field strength from the flux density recorded by NoRP at 35 GHz during peak 4 assuming the emission at this frequency to be optically thin (this seems to be correct in our case, e.g., according to Figure 5). Most parameters seem to be known. The area of the thick target measured from RHESSI 25 – 50 keV images was $A_X \approx 1 \times 10^{18}$ cm^2. We take $\gamma = 2.5$ [$\delta = 4.0$, $B(\gamma - 0.5, 1.5) = 0.267$, and $b(\gamma) = 3.75$], $A_0 \approx 2.2$ photons cm^{-2} keV^{-1} s^{-1} from the HXR spectrum [see (2)]; estimate the $N_r \approx 1.3 \times 10^8$ from expression (7); take a geometrical depth of the emitting source as a square root from its area, and the angle between the line of sight and the magnetic field to be $\approx 60^\circ$ according to the position of the active region. Assuming the total flux to be contributed by two identical footpoint sources in equal magnetic field strengths, we get $B \approx 1200$ G from formulas of Dulk and Marsh (1982). This seems to be plausible taking account of the estimates in Section 2.4. With this magnetic field strength, the frequency maximum is $\nu_{\rm peak} \approx 24$ GHz, which appears to agree with our preliminary conclusions made in Section 2.2.4, but well above the peak frequency shown by the NoRP total flux spectrum (9.4 GHz). Another useful quantity is the maximum flux density $S(\nu_{\rm peak}) \approx 10^{-19} k_{\rm B} \nu_{\rm peak}^2 / c^2 \; (1 - \exp(-2))\, T_{\rm eff}(\nu_{\rm peak}) \tau(\nu_{\rm peak})\, \Omega \;\approx 1500$ sfu where $k_{\rm B}$ is the Boltzmann constant and Ω is the solid angle of one source visible from the Earth. The peak frequency is shown in Figure 10a by the vertical dash-dotted line, and $2S(\nu_{\rm peak})$ is shown by the square. These parameters obviously disagree with the NoRP spectrum (gray). To understand the situation, we model the spectrum of the emitting source at a frequency ν as

$$T(\nu) = T_{\rm eff}(\nu)[1 - e^{-\tau(\nu)}] \tag{8}$$

where $T_{\rm eff}(\nu)$ is the effective temperature of emitting electrons, $\tau(\nu) = \kappa(\nu)L$ is the optical thickness, $\kappa(\nu)$ is the absorption coefficient, and L is the geometrical depth. Both $T_{\rm eff}(\nu)$ and $\kappa(\nu)$ are functions of all parameters of the source determined by formulas of Dulk and Marsh (1982).

The spectrum modeled in this way and converted to the flux density is shown in Figure 10a by a solid black line. It significantly differs from the NoRP spectrum. One might assume that our extension of the approach of Dulk and

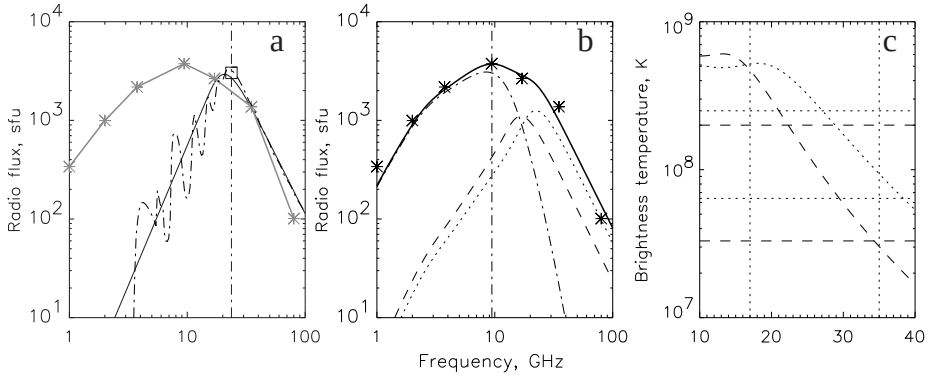

Figure 10. Modeling of the microwave spectrum at Peak 4. (a) The observed NoRP spectrum (gray) and the spectra of two identical footpoint sources modeled using the approach of Dulk and Marsh (black solid) and Ramaty code (dash-dotted). (b) The flux density spectra of the two footpoint sources (dotted and dashed lines) and the looptop part (dash-dotted line), and the total spectrum (thick line). (c) The spectrum of the brightness temperatures for the footpoint sources. Asterisks in panels (a) and (b) show the NoRP measurements, and the vertical dash-dotted lines mark the turnover frequencies.

Marsh (1982) is not justified, e.g., because we have ignored the fact that their expressions loss the accuracy at high (> 100) harmonics of the gyrofrequency and at low (< 10) ones, with the latter being more important in our case.

To verify our results, we have overplotted in the same figure the spectrum calculated using the Ramaty code (Ramaty, 1969; Ramaty *et al.*, 1994) (dashed line). To co-ordinate the different geometries of the sources used in both ways, we have corrected the normalization coefficient for the Ramaty code by a geometrical factor $k_{\rm geom} = 4/(3\sqrt{\pi})$, so that $A_{\rm nor} = N_r \times (\delta - 1) \times (1\,{\rm MeV}/E_r)^{1-\delta}\, ALk_{\rm geom}$ $= 3.5 \times 10^{29}$ electrons MeV^{-1}. Both model spectra satisfactorily agree with each other—of course, without gyroresonance features in the spectrum modeled following Dulk and Marsh (1982), which are indeed not expectable in observations due to inhomogeneity of the magnetic field. Finally, we note that if asymmetric microwave sources were assumed, then the magnetic field strength (and the turnover frequency) for one of them would be still higher.

From comparing the results of the modeling with the observed spectrum, we conclude that an essential emitting component is missing, which is minor at high radio frequencies but dominates at lower frequencies. Even with a frequency-independent brightness temperature, the area of this component must increase with wavelength to partially compensate the decrease of ν^2. Indeed, as known from multi-frequency imaging observations and modeled theoretically, radio-emitting regions expand with wavelength. For example, Bastian, Benz, and Gary (1998) modeled the radio emission of a magnetic loop filled with power-law electrons above a dipole, and the resulting total flux spectrum which they obtained was broad similarly to our situation. Therefore, besides the "kernel" sources emitting at high microwaves and long millimeters, there must be a larger blob covering them, with an area and optical thickness increasing with wavelength. We roughly reproduce the results of Bastian, Benz, and Gary (1998) by combining

the radio-emitting regions from two kernel sources localized in both footpoints of the loop and a blob above them.

We represent the own brightness temperature of a single source 1 at a frequency ν according to (8), and its issue after the passage through another source 2 as $\exp(-\tau_2(\nu))$. Thus, the brightness of a kernel source visible through a blob above it is

$$T(\nu) = T_{\mathrm{eff\,k}}(\nu)\left[1 - e^{-\tau_{\mathrm{k}}(\nu)}\right] e^{-\tau_{\mathrm{b}}(\nu)} + T_{\mathrm{eff\,b}}(\nu)\left[1 - e^{-\tau_{\mathrm{b}}(\nu)}\right]. \qquad (9)$$

We force the area of the blob A_{b} to depend on frequency approximately according to Bastian, Benz, and Gary (1998) and correspondingly change the depth. The magnetic field is also handled as a growing function of frequency. This approach uses the fact that while the frequency decreases, a source becomes thicker, and the contribution from peripheral regions of weaker magnetic fields grows.

The results of the modeling are shown in Figure 10b. First of all, we warn against overestimating these results, because the model is coarse, parameters are not well known, and we therefore did not endeavor to achieve perfect results. The dotted and dashed lines represent the "column" total flux spectra of the two kernel source visible through the loop-associated blob, and the dash-dotted line represents the spectrum of the blob. Panel (c) in the figure shows the brightness temperatures of the kernels. The vertical lines mark 17 and 34 GHz, and the horizontal lines mark the brightness temperatures actually observed in these regions. The relations between the two sources are roughly reproduced at both frequencies, although the brightness temperatures at 17 GHz are higher than the actually observed ones—probably, the sources are not completely resolved at 17 GHz. The flat parts left from the turnover frequencies are due to the contributions from the blob.

We used here $A_0 = 2.2$ photons s^{-1} cm^{-2} keV^{-1} from the observed HXR spectrum, the observed areas of the kernel sources (see Section 2.2.4), and the magnetic field strengths in them of 1350 and 900 G (stronger in S2, because the sources displaced from N1 during peak 4). Their depths were taken as square roots from the areas. The area of the covering blob varied from 7.5×10^{18} cm^2 at 15 GHz up to 5.8×10^{19} cm^2 at 1 GHz, and its depth was taken to be $0.2\sqrt{A_{\mathrm{b}}}$. Accordingly, the magnetic field strength gradually decreased from 530 G to 70 G. Again, we remind of the estimative nature of all the quantities.

With the coarseness of the model, this exercise nevertheless leads to the following undoubted conclusions: (*i*) the broad total flux spectrum could be indeed due to the emission from the whole loop; (*ii*) the peak frequency shown by NoRP does not correspond to real turnover frequencies of the main sources observed at 17 and 34 GHz, being significantly lower; and (*iii*) the parameters of accelerated electrons found from HXR spectra appear to correspond to parameters of microwave-emitting electrons.

Now it is also possible to estimate the power in the accelerated electron flux from (5), which is $\sim 10^{28}$ ergs s^{-1} above 14 keV, and the total energy deposited by accelerated electrons into the thick target during peak 4 (taking its triangular shape and a duration of three minutes) to be $\sim 10^{30}$ ergs. Note that this value is comparable with an estimate of Chandra *et al.* (2006), although they considered

an event with quite different behavior. This value shows again that the energy content in accelerated electrons can be large.

Finally we note that parameters estimated from RHESSI spectra for source S2 at peak 2, $\gamma = 2.8$ and $A_0 = 1.5$, provide a total flux at 35 and 80 GHz close to the observed values with $B \sim 1000$ G.

Two main results come out from our considerations: (*i*) flaring in strong magnetic fields, and (*ii*) essential inhomogeneity of a microwave source — in the sense that different parts of a source dominate its emission at different frequencies. The major warning of our modeling is that the lowness of the peak frequency shown by the total flux spectrum does not guarantee the optically thin regime at 17 GHz or even at 35 GHz. This conclusion is coherent with the assumption of White *et al.* (2003) and hints at another possible reason for the long-standing discrepancy between the power-law indices estimated from HXR and radio data.

3.1.3. The Shoulder and Decay

The behavior of the flux density at long millimeters during the shoulder appears to be intriguing (see Figure 1): the shoulder is pronounced only at lower HXR energies (< 300 keV), which do not significantly affect microwaves, and its intensity is substantially lower than peak 4, whereas the opposite situation occurs at 35 and 80 GHz. As the lower row in Figure 4 shows, flaring is mainly concentrated in S2 at that time, which is nearly similar to the situation during peak 4. The electron spectrum becomes slightly harder (3.85 against 4.0 at peak 4), but this does not seem to be sufficient to explain the observations. A possible solution of this problem might be related to trapping effects. Note also that the relation between the power-law electron indices inferred from HXR and microwave spectra observed at peak 4 and the shoulder (see Figure 8) hints at progressive hardening of microwave-emitting electrons with respect to HXR-emitting ones.

Melrose and Brown (1976) in their trap-plus-precipitation model analytically showed that Coulomb collisions in plasma with a density n_0 significantly affect the "parent" power-law electron spectrum with an index $\delta_{\rm inj}$ injected into a trap so that the number spectrum of trapped electrons transforms into a two-part one separated by a transition energy $E_{\rm T}$. The $E_{\rm T}$ moves right with time t; in the non-relativistic limit, $E_{\rm T} = (3/2\,\nu_0 t)^{2/3}$ with $\nu_0 \approx 5 \times 10^{-9} n_0$ keV$^{3/2}$ s^{-1}. The branches below $E_{\rm T}$ and above it depend on the regime of the injection into the trap. Melrose and Brown (1976) considered, in particular, two limiting injection regimes, i.e., an initial impulsive injection and a continuous one. Metcalf and Alexander (1999) presented in their figures 3 and 4 the spectra calculated for these injection regimes with $\delta_{\rm inj} = 4$ for a parent spectrum, which is close to our case. Schematically, the effects of trapping are as follows.

After an impulsive injection, the electron number spectrum is depleted to harden so that the upper envelope of the whole spectrum goes as $\delta_{\rm inj} - 1.5$, and the branch below $E_{\rm T}$ falls as $E^{5/2}$ towards lower energies. During a continuous injection, the electron number spectrum is augmented to become a broken double-power-law so that the high-energy branch keeps a slope of $\delta_{\rm inj}$ and the low-energy one takes a slope of $\delta_{\rm inj} - 1.5$. The high-energy branch augments

linearly with time. The spectrum of the HXR emission produced by electrons precipitating from a trap in the model of Melrose and Brown (1976) is the same as the thick-target spectrum without trapping due to the steeper spectrum of the collisional precipitation from a trap. These effects altogether result in hardening the spectrum of trapped microwave-emitting electrons with respect to HXR-emitting ones (Melnikov and Magun, 1999).

The case of a continuous injection resembles the progressive hardening of microwave emission observed during the shoulder, especially pronounced in the 80 GHz flux starting from peak 4 by 23:00. The trapping seems to be insignificant at the onset of peak 4, because the polarized emission at 35 GHz closely resembles the 100 – 300 keV light curve (see Figure 1). Then the 80 GHz flux increases almost linearly with time, as expected for a continuous injection in a trap.

An additional support in favor of trapping is provided by a loop-top brightening visible in 34 GHz images obtained during the shoulder and decay (see, e.g., the upper right image in Figure 5). The flat spectrum at 9.4 – 35 GHz during the decay might be due to combined effects of trapping and inhomogeneity of the microwave-emitting source. Both trapped and precipitating electrons can contribute to the microwave emission (Kundu *et al.*, 2001) which makes difficult a more detailed analysis of trapping issues in our event due to insufficient information.

3.1.4. Summary and Consequences

Our analysis has not revealed anything challenging in the event. All the quantities inferred from different observations appear to agree with each. We have not found any conspicuous contradictions. This might be a particularity of this concrete event; on the other hand, a distinctive feature of our study is related to strong magnetic fields. First, MDI magnetograms were recalibrated in October 2007, and this increased the magnetic field strengths by a factor of ≈ 1.7. Second, we applied a projection correction of $1/\cos\vartheta$ (the *zradialize* SolarSoftware function). This correction is generally questionable due to the uncertainty of the orientation of the magnetic field vector; however, the location of the 2003 June 17 flare sources just above sunspots justifies the "radialization". The corresponding correction factor is from 1.82 for sunspot N1 up to 1.93 for S2. Thus, we have dealt with magnetic fields three times stronger than uncorrected ones. Such a correction factor appears to be significant for magnetic fields themselves; it rather becomes crucial in interpretation of the gyrosynchrotron emission. We now illustrate what one would see if the magnetic fields in the event were thought to be 2 – 3 times weaker.

1. The underestimation of the magnetic field strength immediately results in an underestimate of the microwave peak frequency that obtains a deceiving confirmation from NoRP total flux spectra.
2. Consequently, radio frequencies which do not correspond to the optically thin regime are misinterpreted to belong to the optically thin limit. There is no reason to use problematic 80 GHz records in this case, and the microwave spectrum estimated from the 35 to 17 GHz ratio inevitably becomes flatter than the optically thin one. The discrepancy with the HXR spectrum naturally appears.

3. Believing that the 17 GHz emission belongs to the optically thin regime, one gets a strange behavior of the polarization.
4. With the underestimated magnetic field, one gets a significant deficiency of the flux density, and is constrained to search for a way to increase it.
5. The Razin effect seems to become important at higher frequencies than it in reality does. It was most likely negligible in our event.

These considerations might provide a key to reconcile some puzzling issues established in several other events. As a by-product of our analysis we conclude that the re-calibrated MDI magnetograms appear to be more consistent with microwave data than the former ones.

3.2. Outline of the Event

The event appears to be prepared by the preceding evolution of AR10386. The most conspicuous are the emergence of sunspot S1 close to sunspot N1 and the persistent motion of S2 southwest, towards the southern region SR. A system of filaments formed above the main neutral line in the active region.

The onset of the event was probably related with the activation and eruption of filaments, whose brightening and gradual rise started nearly simultaneously with an increase of the soft X-ray flux. The brightening of the filament and the SXR emission around it indicate heating in this region that implies energy release in the corona. Then the filaments unbent to become vertical. When their northern ends reached a significant height, the HXR flux also started to rise. Finally, the filaments abruptly erupted, and the HXR peak 1 occurred at the same time. This chain of events basically corresponds to a "standard" picture of an eruptive event, which also seems to agree with subsequent phenomena.

An arcade of flare loops evolved along the previous position of the filaments (most likely above the main neutral line). At the basis of the arcade, the TRACE 195 Å images also show bright kernels spatially corresponding to the major flare sources visible in HXR and microwaves. Two of these sources were located at basis of pre-eruptive filaments. A distinct feature of this flare was its occurrence just above sunspots, including their umbrae. The strongest emissions at highest energies were observed when flaring occurred above sunspots, i.e., in strongest magnetic fields.

As already mentioned this flare is one of the few observed by RHESSI with good photon counts in the 300 – 800 keV range, and it was possible to map up to 400 keV. Two strong HXR and microwave footpoint sources above sunspots dominated throughout the event. The 300 – 800 keV emission was strongest at peak 4. We find that at all peaks the HXR sources had nearly the same positions. We find power law electron energy spectral index delta ~ 4.0 during each peak with no obvious hardening from one peak to another. This implies that the acceleration mechanism was the same for different peaks – no additional acceleration was needed for different peaks. The flare source in energy bands from 25 to 400 keV coincided within $1''$at the onset of peak 4. This suggests that the acceleration process must be the same for all energy levels – from 25 to 400 keV. Grigis and Benz (2008) from their study of the spectral evolution of HXR bursts also concluded that the observed spectral changes occur due to "gradual

change in the accelerator" rather than contribution from different acceleration mechanisms. Our results appear to be coherent with this conclusion, although they do not seem to confirm the model proposed by Grigis and Benz (2008).

In terms of magnetic reconnection models (e.g., Forbes and Priest, 1995), one might indeed expect the flaring to be strongest above sunspots and especially their umbrae. Several authors (e.g., Qiu *et al.*, 2002; Asai *et al.*, 2004) found a correlation between the energy release rate computed from footpoint motions across the magnetic fields and intensities of flare emissions in HXR and microwaves. A similar correlation probably would exist for the event under discussion. However, existing flare models do not seem to predict various properties of a flare revealed in our paper, e.g., whether a flare would enter a sunspot, how hard the electron spectrum could be, etc. It is not clear why the spectrum of the source above sunspot N1 initially was very soft and significantly hardened later on, whereas the source above sunspot S2 persistently had the hardest spectrum all over the flare (excluding peak 1, which we did not analyze for incomplete information).

A class of flares occurring above the sunspot umbrae does not seem to be sufficiently studied, and their properties have not been well established. Note that the analysis of a 2005 January 20 extreme event lead Grechnev *et al.* (2008) to a conclusion that its extremeness was due to the occurrence of the flare above the sunspot umbrae. One of features observed in that flare was a large SXR-emitting loop-like structure rooted in the umbrae. Such a loop between sunspots N1 and S2 was also observed in our 2003 June 16 flare (see Figure 3f). Total magnetic flux was mainly concentrated between two umbrae, unlike widespread magnetic fields in a typical flare. This feature appears to be expectable: large total magnetic flux outgoing from a sunspot must be balanced by incoming flux at the other end of a loop that is favored by the presence of another sunspot. However, this is one of only few expected properties of sunspot-associated flare.

4. Conclusion

Our multi-spectral analysis of the 2003 June 17 event has shown that its main features were probably related to the location of main flare sources above sunspots. This determines strong microwave flare emissions and probably was somehow related to hard electron spectra observed in the event. Properties of flare emissions imply a single acceleration mechanism, which was most likely the same for all energy domains up to 800 keV, and we have not found any indications of a second-step acceleration. Some features of microwave emissions appear to be indicative of trapping issues, consistent with existing concepts. However, we have not found a challenging discrepancy between the spectra of electrons responsible for microwaves and hard X-rays repeatedly reported in previous studies. Instead, we propose that sometimes this discrepancy could be due to underestimations of the microwave turnover frequency, which could be low due to the inhomogeneity of the microwave/millimeter source. So we emphasize that the microwave peak frequency measured from total flux records does not guarantee the optically thin regime of sources observed at higher frequencies. It rather shows the lower limit of possible turnover frequencies of gyrosynchrotron spectra of footpoint-associated

sources. This is also related to probable underestimations of the magnetic field strength. This conclusion appears to be coherent with results of White *et al.* (2003) which implied optically thick regime even at 35 GHz, although their event was significantly different. These issues highlight the importance of total flux measurements of radio bursts in the millimeter range. Our results also emphasize the importance of both experimental and theoretical analyses of sunspot-associated flares, which might be related to extreme solar events, but do not appear to be sufficiently studied.

Acknowledgements We thank A.M. Uralov, A.T. Altyntsev, and H.S. Hudson for useful discussions. We thank the instrumental teams of the TRACE mission, MDI on SOHO, the Nobeyama Solar Facilities, the Big Bear Solar Observatory, and the GOES satellites.

The research of MRK and SMW for this paper was supported by NSF grant ATM 02–33907 and NASA grants NAG 5–12860 and NNG05–GI–91G. The research of EJS was supported by NASA grants NAG 5–10180 and NNG06–GB–636. The research of VVG and NSM was supported by the Russian Foundation of Basic Research under grant 07–02–00101.

References

Asai, A., Yokoyama, T., Shimojo, M., Masuda, S., Kurokawa, H., Shibata, K.: 2004, *Astrophys. J.* **611**, 557.
Bastian, T. S., Benz, A. O., Gary, D. E.: 1998, *Ann. Rev. Astron. Astrophys.* **36**, 131.
Bogachev, S. A., Somov, B. V.: 2001, *Ast. Let.* **45**, 157.
Bogachev, S. A., Somov, B. V.: 2007, *Ast. Let.* **33**, 54.
Brown, J. C.: 1971, *Solar Phys.* **18**, 489.
Chandra, R., Jain, R., Uddin, W., Yoshimura, K., Kosugi, T., Sakao, T., Joshi, A., Deshpande, M. R.: 2006, *Solar Phys.* **239**, 239.
Dulk, G. A.: 1985, *Ann. Rev. Astron. Astrophys.* **23**, 169.
Dulk, G. A., Marsh, K. A.: 1982, *Astrophys. J.* **259**, 350.
Forbes, T. G., Priest, E. R.: 1995, *Astrophys. J.* **446**, 377.
Grechnev, V. V.: 2003, *Solar Phys.* **213**, 103.
Grechnev, V. V., Kurt, V. G., Chertok, I. M., Uralov, A. M., Nakajima, H., Altyntsev, A. T., Belov, A. V., Yushkov, B. Yu., Kuznetsov, S. N., Kashapova, L. K., Meshalkina, N. S., Prestage, N. P.: 2008, *Solar Phys.* **252**, 149.
Grigis, P. C., Benz, A. O.: 2008, *Astrophys. J.* **683**, 1180.
Handy, B. N., Acton, L. W., Kankelborg, C. C., Wolfson, C. J., Akin, D. J., Bruner, M. E., Caravalho, R., Catura, R. C., *et al.*: 1999, *Solar Phys.* **187**, 229.
Hudson, H. S., Canfield, R. C., Kane, S. R.: 1978, *Solar Phys.* **60**, 137.
Hudson, H. S., Wolfson, C. J., Metcalf, T. R.: 2006, *Solar Phys.* **234**, 79.
Ji, H., Huang, G., Wang, H.: 2007, *Astrophys. J.* **660**, 893–900.
Kundu, M. R., White, S. M., Gopalswamy, N., Lim, J.: 1994, *Astrophys. J. Supp.* **90**, 599.
Kundu, M. R., Nitta, N., White, S. M., Shibasaki, K., Enome, S., Sakao, T., Kosugi, T., Sakurai, T.: 1995, *Astrophys. J.* **454**, 522.
Kundu, M. R., White, S. M., Shibasaki, K., Sakurai, T., Grechnev, V. V.: 2001, *Astrophys. J.* **547**, 1090.
Lee, J., Gary, D. E., Shibasaki, K.: 2000, *Astrophys. J.* **531**, 1109.
Lin, R. P., Dennis, B. R., Hurford, G. J., Smith, D. M., Zehnder, A., Harvey, P. R., *et al.*: 2002, *Solar Phys.* **210**, 3.
Melnikov, V. F., Magun, A.: 1998, *Solar Phys.* **178**, 153.
Melrose, D. B., Brown, J. C.: 1976, *Mon. Not. Roy. Astron. Soc.* **176**, 15.
Metcalf, T. R., Alexander, D.: 1999, *Astrophys. J.* **522**, 1108.
Metcalf, T. R., Alexander, D., Hudson, H. S., Longcope, D. W.: 2003, *Astrophys. J.* **595**, 483.

Nakajima, H., Sekiguchi, H., Sawa, M., Kai, K., Kawashima, S.: 1985, *Publ. Astron. Soc. Japan* **37**, 163.
Nakajima, H., Nishio, M., Enome, S., Shibasaki, K., Takano, T., Hanaoka, Y., Torii, C., Sekiguchi, H., *et al.*: 1994, *Proc. IEEE* **82**, 705.
Preka-Papadema, P., Alissandrakis, C. E.: 1992, *Astron. Astrophys.* **257**, 307.
Qiu, J., Lee, J., Gary, D. E., Wang, H.: 2002, *Astrophys. J.* **565**, 1335.
Ramaty, R.: 1969, *Astrophys. J.* **158**, 753.
Ramaty, R., Schwartz, R. A., Enome, S., Nakajima, H.: 1994, *Astrophys. J.* **436**, 941.
Scherrer, P. H., Bogart, R. S., Bush, R. I., Hoeksema, J. T., Kosovichev, A. G., Schou, J., *et al.*: 1995, *Solar Phys.* **162**, 129.
Silva, A. V. R., Wang, H., Gary, D. E.: 2000, *Astrophys. J.* **545**, 1116.
Takasaki, H., Kiyohara, J., Asai, A., Nakajima, H., Yokoyama, T., Masuda, S., Sato, J., Kosugi, T.: 2007, *Astrophys. J.* **661**, 1234.
Torii, C., Tsukiji, Y., Kobayashi, S., Yoshimi, N., Tanaka, H., Enome, S.: 1979, *Proc. Res. Inst. Atmospherics* **26**, Nagoya Univ., 129.
White, S. M.: 2009, Reconciliation of hard X-ray and microwave spectra, in: RHESSI book, Chapter ??
White, S. M., Krucker, S., Shibasaki, K., Yokoyama, T., Shimojo, M., Kundu, M. R.: 2003, *Astrophys. J. Lett.* **595**, 111.
White, S. M., Kundu, M. R.: 1997, *Solar Phys.* **174**, 31.
White, S. M., Thomas, R. J., Schwartz, R. A.: 2005, *Solar Phys.* **227**, 231.
Wild, J. P., Smerd, S. F., Weiss, A. A.: 1963, *Ann. Rev. Astron. Astrophys.* **1**, 291.
Zheleznyakov, V. V. Radio emission of the Sun and planets: 1969, Oxford, New York, Pergamon Press, 1st ed.